Molecular Crystals and Liquid Crystals

Publication details, including instructions for authors and subscription information:
http://www.tandfonline.com/loi/gmcl20

Nanostructured Surfaces: Scientific and Optical Device Applications

Charles Rosenblatt [a]

[a] Department of Physics, Case Western Reserve University, Cleveland, Ohio, U.S.A.

Version of record first published: 18 Oct 2010

To cite this article: Charles Rosenblatt (2004): Nanostructured Surfaces: Scientific and Optical Device Applications, Molecular Crystals and Liquid Crystals, 412:1, 117-134

To link to this article: http://dx.doi.org/10.1080/15421400490439734

Mol. Cryst. Liq. Cryst., Vol. 411, pp. 117/[1727]–134/[1744], 2004

ISSN: 1542-1406 print/1563-5287 online
DOI: 10.1080/15421400490439734

Taylor & Francis
Taylor & Francis Group

NANOSTRUCTURED SURFACES: SCIENTIFIC AND OPTICAL DEVICE APPLICATIONS

Charles Rosenblatt
Department of Physics, Case Western Reserve University, Cleveland, Ohio 44106-7079, U.S.A.

Surfactant and polymer-coated substrates may be patterned on microscopic and nanoscopic length scales by the stylus of an atomic force microscope. The resulting easy axes control the director orientation, facilitating both scientific studies and technological devices that were not possible using previous techniques. In this talk I will present a review of work from my laboratory, performed in collaboration with Milind P. Mahajan, Wen Bing, Ghanshyam P. Sinha, and Rolfe G. Petschek, along with colleagues L.V. Mirantsev (St. Petersburg, Russia) and Jong-Hyun Kim and Hiroshi Yokoyama (Tsukuba, Japan). Work includes a number of optical gratings for beam steering applications, gray scale images, anchoring strength studies, effects of controlled surface roughness on smectic order, and nanoscopic elasticity and anchoring effects on the nematic-isotropic phase transition.

Keywords: atomic force microscope; gratings; nanostructured liquid crystals; substrate manipulation

With the invention of the scanning tunneling microscope (STM) and its offsprings the atomic force microscope (AFM) and near-field scanning optical microscope (NSOM), a revolution has occurred in the way that we view and manipulate materials [1,2]. These instruments are capable of obtaining topographical, magnetic, and adhesive force information on atomic length scales. One of the earliest and still most common applications of SPM techniques to the field of liquid crystals is the study of the topography of the treated substrate [3], particularly the polymer that is rubbed to induce planar alignment. For example, AFM studies of the substrate have

This work was supported by the National Science Foundation under grant DMR89-20147 and by the U.S. Department of Energy under grant DE-FG02-01ER45934. Acknowledgment is also made to the Donors of the Petroleum Research Fund, administered by the American Chemical Society, for partial support of this research under grant 37736-AC7.

Address correspondence to Charles Rosenblatt, Deptartment of Physics, Case Western University, Cleveland, OH 44106-7079, U.S.A.

examined [4–6] the issue of the liquid crystal alignment mechanism [7,8]. Other studies have examined the relationship between the topography of the rubbing fiber and the topography it induces in the polymer surface [9], the effects of multiple rubbings along different directions [10,11], and the topography of a surface that is subjected to polarized ultraviolet light [12,13]. The structure of liquid crystal ordering itself also has been examined by SPM techniques in very diverse settings, such as a smectic A liquid crystal at a smooth substrate (such as graphite) [14,15], and a free-standing smectic C liquid crystal film transferred to a self-assembled monolayer-coated glass [16]. Although these techniques have helped us to better understand the phenomenon of uniform alignment and molecular order, they have not created *new* liquid crystal phenomena—

—Until recently. Since 1994 AFM nanolithography techniques [17,18] have been applied to liquid crystals, whereby the stylus is used to manipulate polymer-coated substrates on length scales ranging from several micrometers down to nanometers. Rüetschi *et al.* [17] and Pidduck *et al.* [18] showed that the resulting nanoscopic substrate patterns align the liquid crystal director along the local "writing" direction of the stylus. Kim *et al.* recently demonstrated that bistable director orientation may be achieved with tiny pixel sizes [19]. Although much emphasis was placed on the writing-induced topography, recently we have found that very "light writing," *i.e.*, using a small force, results in liquid crystal alignment even though no topographical changes could be detected [20]. Based on the technique of AFM nanolithography, also known as "AFM writing," we have been engaged in a dual program of scientific discovery and technological development that exploits our ability to create extraordinarily tiny pixels. Our earliest work dealt with the basic principles underlying the technique [21], and more recently with the copious scientific phenomena—this includes elasticity, surface interactions, and phase transitions [22,23]—associated with liquid crystals that may be controlled and explored on nanoscopic length scales. Additionally, AFM writing as applied to liquid crystals offers many technological possibilities, including devices for optical beam steering and wavelength demultiplexing in the broad field of "optical communications" and nano-patterned chemical and biological sensors. These technologies exploit the small length scales of director orientation and large liquid crystal optical anisotropy, providing a host of new applications. This paper presents an overview of some of our scientific and technological work to date.

If a polyimide is spin-coated onto a substrate—either directly onto glass or onto a semitransparent layer of electrically-conducting indium-tin-oxide (ITO)—and is unidirectionally rubbed, it forms a template for alignment of the liquid crystal director. Although rubbing is most often performed with a cotton cloth that covers a large area, it has been shown that a spatially

periodic rubbing of the polyimide layer with the stylus of an atomic force microscope may accomplish the same task [17–19,22]. Figure 1a shows an image of a topographically-smooth polyimide layer rubbed with a silicon AFM stylus under "hard rubbing" conditions, with a force of approximately 5 μN; the spacing between grooves is approximately 50 nm. Figure 1b shows grooves spaced 25 nm apart on a topographically rougher polyimide surface. Our data, moreover, show that very "light rubbing" can also achieve excellent alignment of the liquid crystal, albeit with weaker anchoring conditions. In practice, we can achieve rub line spacings L of a few nanometers.

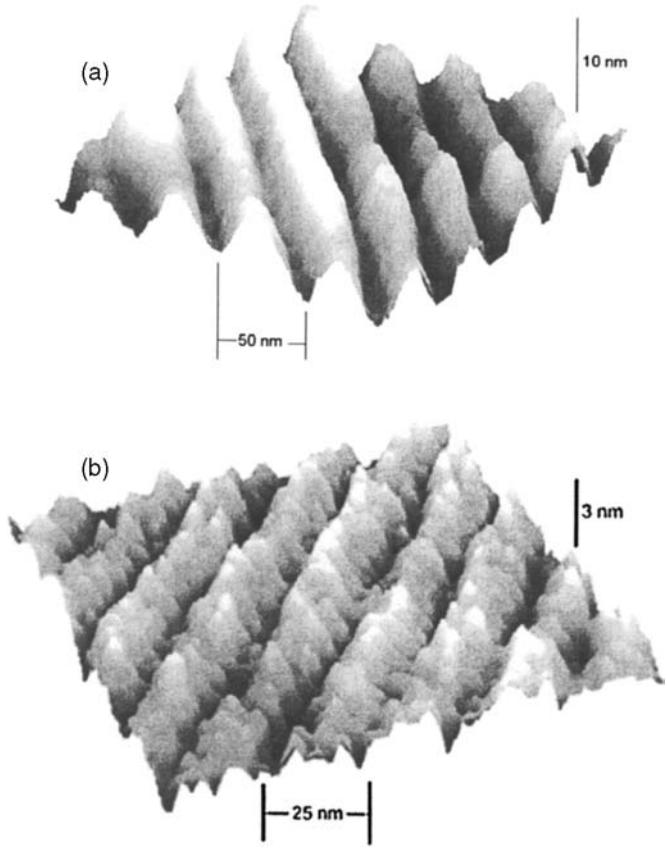

FIGURE 1 AFM-rubbed polyimide. The polyimide was scored with the stylus in contact mode, and the image of the grooved surface is then created by the same stylus in non-contact ("tapping") mode. a) Grooves written 50 nm apart on smooth surface. b) Grooves spaced 25 nm on a rough surface.

Having demonstrated that AFM-writing can control both the anchoring and alignment for large pixels (~10 μm), we examined the possibility of writing patterns on much smaller length scales, with pixel sizes of a few micrometers down to approximately 100 nm. Depending upon the thickness of the cell and the anchoring strength at the substrates, the liquid crystal director at the substrate is approximately parallel to the local easy axis. Figure 2 shows a typical rubbing pattern on a polyimide-coated surface. The pixels correspond to long stripes of width 3 μm, such that each pixel consists of several rub lines spaced approximately 500 nm apart. [In order to optically image the liquid crystal cell under the microscope, large pixels were used for purposes of demonstration. Much smaller pixel sizes ($\gtrapprox$100 nm) and spacings between rub lines (L $\gtrapprox$ 10 nm) are routinely achieved, although the resulting effect on the liquid crystal is difficult to image optically]. Based on our ability to create tiny pixels, each having a different easy axis φ_o for liquid crystal orientation, we constructed a cell in which one polyimide-coated surface was scribed unidirectionally within each pixel by an AFM stylus, and the other surface was treated for spatially-uniform *homeotropic* alignment. The rubbing direction φ_o within each pixel was easily controlled (Figs. 2 and 3). When the cell was filled with a nematic liquid crystal and placed between crossed polarizers, the transmitted intensity I of the pixel is given by $I \propto \frac{1}{2}(1 - cos\,\alpha)sin^2 2\beta$ [Ref. 21], where the optical retardation $\alpha = \int_0^d \frac{2\pi}{\lambda}\Delta n(z)dz$, β is the angle

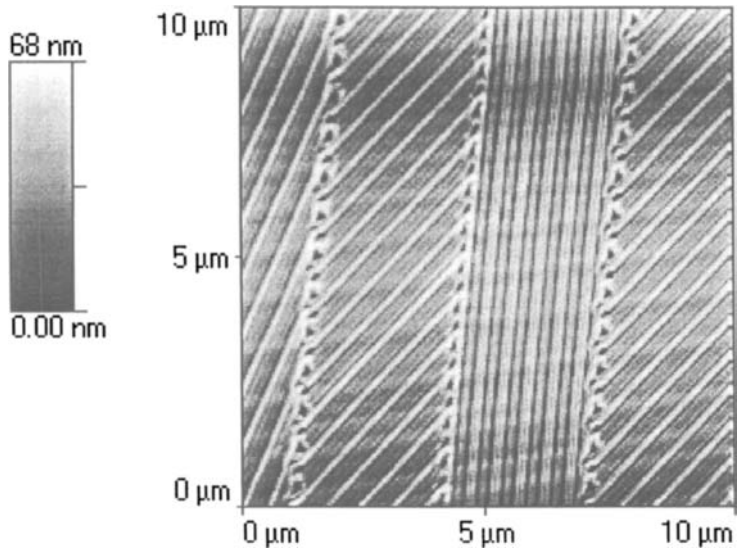

FIGURE 2 Rubbing pattern for long pixels, each of width 3 μm.

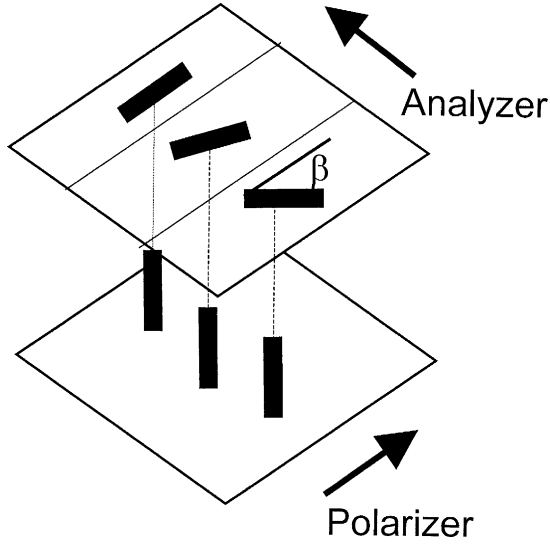

FIGURE 3 Schematic representation of hybrid cell. AFM image of upper substrate is shown in Figure 2.

between the polarizer (or analyzer) and the rubbing direction of the pixel, Δn the birefringence, λ the wavelength of light, and d the cell spacing. Figure 4 shows a liquid crystal cell with three gray levels and a contrast ratio >20; the striped pixels are based upon rubbing at angles $\beta = 0^\circ$, 45°, 22.5°, 45°, $0^\circ, \ldots$ with respect to the polarizer. Smaller pixels of width several hundred nm also have been created, although such small pixels cannot easily be imaged with an optical microscope. Instead, the efficacy of those cells is examined by diffraction. A particularly useful feature of this architecture is that, by using substrates coated with semitransparent ITO, one can electrically-manipulate the brightness and contrast of the image. These many desirable attributes notwithstanding, one must bear in mind that AFM writing with a single-stylus is very slow. For commercial viability, then, massively parallel writing (*using* an array of styli) may be implemented. Alternatively, we may use single-stylus AFM writing as a tool to facilitate *very* rapid prototyping of new device ideas, which can then be implemented on a large scale using other nanolithographic techniques.

Along similar lines we have developed a new optical grating technique based upon the light's polarization state, rather than its amplitude or phase [24]. One substrate of the liquid crystal cell is uniformly rubbed for planar alignment. The other surface is rubbed along a specific direction β_{oj} in each pixel j (Fig. 5). Linearly polarized light entering the cell along the uniform rubbing direction is locally *rotated* by the liquid crystal, emerging from the

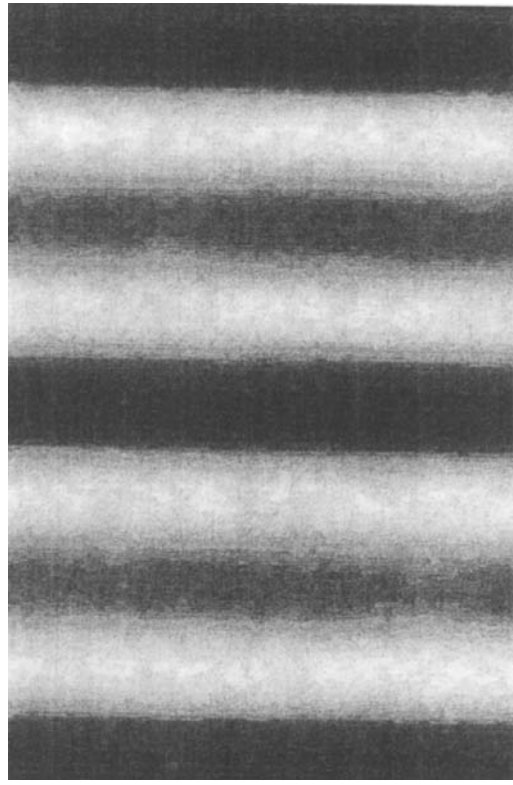

FIGURE 4 Scanned image of Polaroid photograph of thick (3 μm) cell, based on Figures 2 and 3. Stripes are 3 μm wide. Note that pixel definition is actually far better than could be reproduced on this page.

cell with a given polarization orientation. The x- and y-components of polarization interfere separately, giving rise to interference patterns that depend on the polarization state of the emerging light. For the pattern shown in Figure 5, only odd diffraction orders appear (Fig. 6). In another embodiment, if light were to enter the cell polarized at 45° with respect to the uniform rubbing direction, the light would break into two eigenmodes—ordinary and extraordinary—each of which would rotate along with the director. Moreover, there also would be a net phase retardation of one polarization with respect to the other as the light emerges from the cell. By judicious selection of the rubbing angles β_{oj} and the overall cell thickness, we can arrange that the emerging light from each pixel be circularly polarized and have a phase β_{oj}–$\beta_{o(j-1)}$ with respect to the adjacent pixel. Taking this idea one step further, a particularly

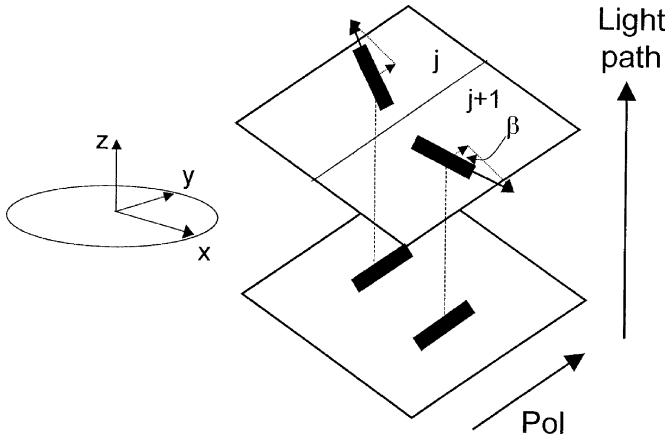

FIGURE 5 Schematic diagram of simple polarization grating. y-component of polarization is undiffracted, x-component is diffracted (see Figure 6).

interesting scenario is for β_o to vary from -180° to $+180^\circ$ over a given distance, and then the pattern is repeated over and over. Figure 7 shows part of this pattern, *i.e.*, $-90^\circ \lessapprox \beta_o \lessapprox +90^\circ$. [In practice the full 360° range of β_o

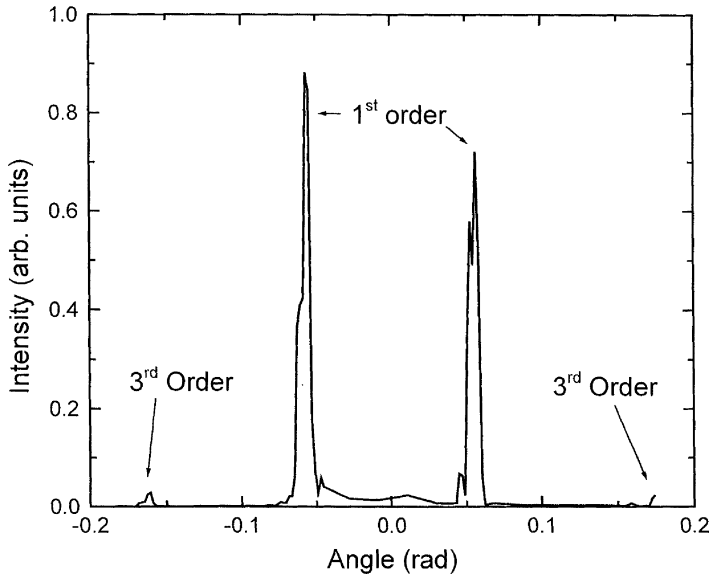

FIGURE 6 Diffraction pattern based on Figure 5. Notice that only odd orders appear.

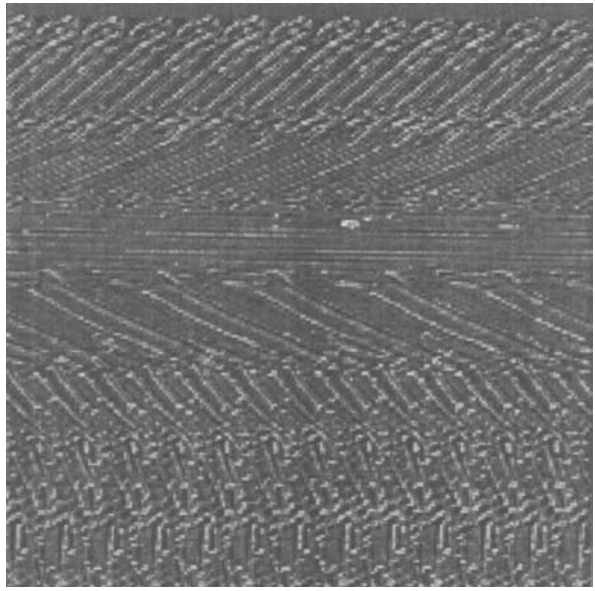

FIGURE 7 AFM writing pattern, producing an easy axis angle β_o that varies linearly with position. Shown here is one half of a period, where each horizontal striped pixel of approximately 225 nm in width is composed of rub lines of separation $\sim$50 nm.

cannot be achieved, although we have successfully varied β_o from -160° to $+160^\circ$ in steps of 10°]. This architecture is equivalent to a "blazed grating" specifically for circularly polarized light, and allows the optical beam to be electrically-switched between direct throughput and a *single* diffraction spot. We have constructed several prototypes exhibiting diffraction peaks at angles up to 5°. We are currently developing a switchable blazed grating that operates independently of the optical polarization.

The AFM-based lithographic technique is extremely powerful for developing electrooptical devices having pixel sizes in the 100 nm range. Its utility, however, goes well beyond device applications, and opens a new array of scientific phenomena. One question that we have addressed is why liquid crystal alignment still takes place even if a small region ($\sim$a few hundred nm) of the substrate is completely missed during the rubbing process. We explored both the polar and azimuthal anchoring characteristics at the interface for a polyimide rubbed with an AFM stylus, with emphasis on the effect of the spatial separation L between rub lines.

Two types of cells were used. For measurements of polar anchoring strength W_θ, two indium-tin-oxide coated glass substrates were cleaned. One substrate was coated with a monolayer of the surfactant hexadecyltri-

methylammonium bromide (HTAB) to induce homeotropic alignment; the other substrate was spin coated with DuPont polyimide PI-2555 and baked. The polyimide-coated substrate was then rubbed along one axis over a $100 \times 100\,\mu m$ area by the stylus with a constant force of $5\,\mu N$, resulting in grooves of width $w_o \sim 40\,nm$ and depth $h_o \sim 10\,nm$. (This was determined by noncontact atomic force microscopy). The center-to-center separation L of rub lines in a given square was examined in the range $0.2 < L < 4.0\,\mu m$. The regions between the rub lines were left unrubbed. The two substrates were then placed together to form a cell. This homeotropic-planar hybrid cell was filled in the isotropic phase with pentylcyanobiphenyl (5CB) and allowed to cool to room temperature. Several such cells were prepared, one for each value of L. For measurements of azimuthal anchoring strength W_φ, both substrates were coated with the polyimide PI-2555; one substrate was buffed by a cotton cloth and the other scribed with the AFM. This substrates were placed together to form a twist cell with the two rubbing directions forming an angle $\beta = 84^\circ$, cemented, and filled with 5CB. Experimental details of the anchoring strength measurements may be found in Ref. 22.

Figures 8 and 9 show the effective polar and azimuthal anchoring strength coefficients, respectively, where "effective" is defined as the anchoring strength spatially averaged over the rub region. The pairs of data

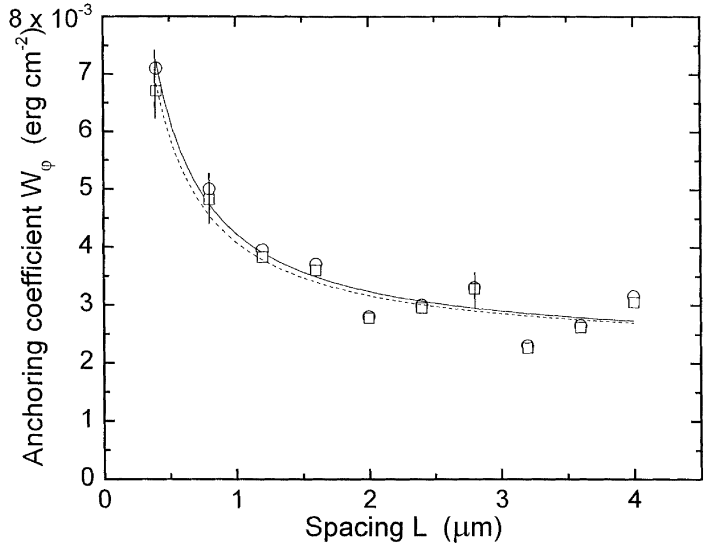

FIGURE 8 Effective polar anchoring strength W_φ. Squares correspond to infinite W_c and circles to $W_c = 0.1\,erg\,cm^{-2}$. Dashed lines correspond to fitted values for infinite W_c and solid line to fitted values for $W_c = 0.1\,erg\,cm^{-2}$.

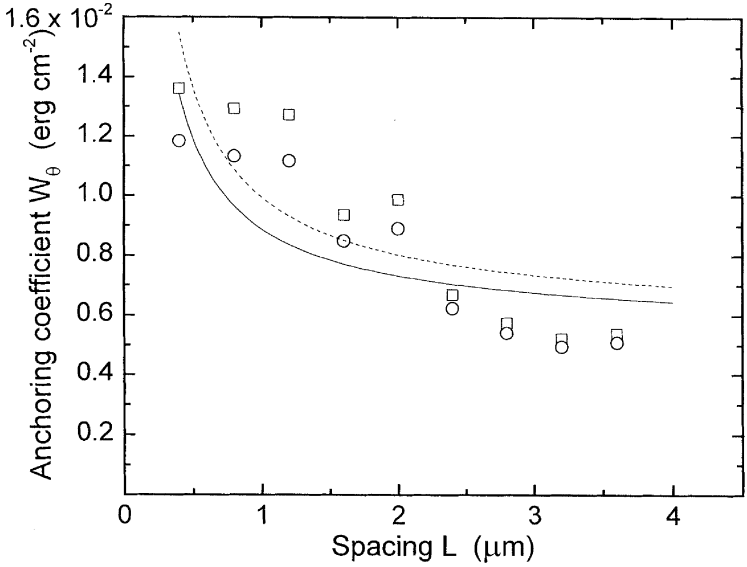

FIGURE 9 Effective polar anchoring strength W_θ. Squares correspond to infinite W_u and circles to $W_u = 0.1\,\mathrm{erg\,cm^{-2}}$. Dashed lines correspond to fitted values for infinite W_u and solid line to fitted values for $W_u = 0.1\,\mathrm{erg\,cm^{-2}}$.

points and fits represent two different assumptions about the anchoring of the opposing substrate: either an infinite anchoring strength or an anchoring strength of $0.1\,\mathrm{erg\,cm^{-2}}$. Assuming zero anchoring strength in the unrubbed regions, the effective azimuthal and polar anchoring strengths would be the ratio of the area of the rub lines to the total surface area of the cell, decreasing with L as w_o/L. Figures 8 and 9, however, show a slower falloff with L. To understand this phenomenon, we invoke the surface memory effect (SME) [25–28]. In the SME liquid crystal molecules achieve an orientation that may be different from the original easy axis of the substrate. This comes about because of an elastic torque imposed on the liquid crystal by another part of the substrate, an opposing substrate, or by some external field. Although the mechanism is not fully understood, the existence of an SME is well documented. If we assume that our effective anchoring strength can be described by a spatially averaged anchoring strength due to the rubbed region and the anchoring in the unrubbed region—this is where the SME plays an important role—the *effective* anchoring strength coefficient is

$$W = W_1\left(\frac{w_o}{L}\right) + W_2\left(\frac{L - w_o}{L}\right) + \frac{2W_3}{L}\int_{w_o/2}^{L-w_o/2} exp\left(\frac{-xW_2}{K}\right)dx \qquad (1)$$

where W corresponds to the appropriate (polar or azimuthal) anchoring strength coefficient. The first term corresponds to the anchoring contribution from the rubbed region weighted by its fractional area, where W_1 is the anchoring strength coefficient of that region. The second term corresponds to the inherent anchoring strength of the unrubbed region weighted by its area; this corresponds to most of the sample surface. Although $W_{\varphi,2}$ for the case of azimuthal anchoring is expected to be very small, $W_{\theta,2}$ for polar anchoring is likely to make an important contribution to the overall anchoring of the surface [29,30]. The third term has an *ad hoc* form and is due to the SME. We assume that the ordering in the rubbed region is strong and is transmitted elastically along the surface into the unrubbed region over a distance of order $\xi = K/W$, where K is the appropriate elastic constant. Over time this induced order creates a SME in the unrubbed region, giving rise to an additional contribution W_3. This contribution is strongest in the vicinity of the rub lines, and decays to zero on a length scale ξ into the unrubbed region. The factor of 2 is due to each unrubbed region being affected by the two rub lines that border that region.

Let us first consider the W_φ in Figure 8, and use Eq. (1) to fit the data. Assuming that the anchoring strength W_c at the opposing substrate is infinite (squares in Fig. 8), we find that $W_{\varphi,1,} = (0.048 \pm 0.004)$, $W_{\varphi,2} = (0.0016 \pm 0.002)$ and $W_{\varphi,3.} = (0.0008 \pm 0.001)\,\mathrm{erg\,cm^{-2}}$, respectively. For $Wc = 0.1\,\mathrm{erg\,cm^{-2}}$ (circles), the corresponding values are 0.052, 0.0019, and 0.0004, with similar error bars. Although $W_{\varphi,1}$, which is associated with the rub lines, is much larger than that in the unrubbed regions, it rapidly becomes less important with increasing L. Additionally, because $K/W_{\varphi,2} \sim 4\,\mu m$, the SME extends a long distance from the rub line, and the induced anchoring due to the SME tends to be uniform over the entire unrubbed region. It is therefore difficult to separate out experimentally the spatially-uniform "bare" anchoring component $W_{\varphi,2}$ from the weakly spatially-varying SME component of anchoring. On the other hand, if we assume that $W_{\varphi,2} \sim 0$, we find that the fitted values of $W_{\varphi,1}$ remain nearly unchanged and the SME component in the unrubbed region increases. Moreover, the curve's shape is nearly unchanged. Thus, we believe that a more realistic set of values for $W_{\varphi,1,}$, $W_{\varphi,2,}$, and $W_{\varphi,3}$ are respectively ~ 0.05, ~ 0, and $\sim 0.002\,\mathrm{erg\,cm^{-2}}$, with the SME playing the major role in the unrubbed region.

We now turn to the polar anchoring data in Figure 9. With $W_u = \infty$ (squares), we find that $W_{\theta,1}$, $W_{\theta,2,}$ and $W_{\theta,3}$ are 0.099, 0.0033, and $0.00031\,\mathrm{erg\,cm^{-2}}$, respectively. Note that the azimuthal fit is superior to the polar fit, in part owing to the more difficult task of measuring the anchoring strength coefficient when anchoring is strong. Thus, we must apply an uncertainty of at least $\pm 25\%$ to the polar results. We believe that the relatively poor *form* for the polar fit is an artifact of the larger polar

anchoring strength, whereby small systematic measurement errors propagate into large errors in the derived quantity W_θ. For $W_u \sim 0.1\,erg\,cm^{-2}$ (circles), the three anchoring coefficients in Eq. (1) are 0.081, 0.0031, and $0.00029\,erg\,cm^{-2}$, respectively, with similar error bars. Obviously, $W_{\theta,1} > W_{\varphi,1}$. Of more interest is the anchoring in the unrubbed region. We would expect to observe a significant, nonzero value for $W_{\theta,2}$, which seems to be the case here. Because of the larger value of $W_{\theta,2}$ and the smaller value of K_θ, the ratio $K_\theta/W_{\theta,2}$ is only of order 1 μm. Thus, the SME extends only a short distance from the rub lines and plays a smaller role than it does for the azimuthal anchoring.

We draw several conclusions. First, both $W_{\theta,1}$ and $W_{\varphi,1}$ in the rubbed regions are moderately strong, of order 0.05 to $0.1\,erg\,cm^{-2}$. Second, the effective anchoring strength coefficients decrease with increasing spacing L, *but they do not appear to asymptotically approach zero*. For small spacings W_θ and W_φ decrease as w_o/L; for larger spacings the small anchoring strength contributions from the unrubbed regions play a larger role in the spatially-averaged values of W_θ and W_φ. For azimuthal anchoring, we would expect that the bare anchoring strength $W_{\varphi,2} \sim 0$, and therefore $W_{\varphi,3}$, which is induced by the SME, would play the predominant role for large separations. For polar anchoring, $W_{\theta,2} > 0$; this has two principal effects: It makes an important contribution W_θ when L is large, and it limits the region that may be affected by the SME. Aside from the fundamental mechanism, these results indicate that spatially-periodic rubbing be used to control the anchoring strength. Unlike buffing with a cotton cloth, the spacing between rub lines is easily controlled, and can be used to simulate various anchoring conditions.

Let us now turn to the effects of controlled surface roughness on smectic order. Substrate-induced smectic order in the nematic phase grows at a flat substrate into the bulk to a depth of order the smectic correlation length, thereby reducing the effective nematic region that may be deformed in a Fréedericksz transition and increasing the threshold field [31]. However, this surface-induced smectic order may be suppressed by nanoscopic surface corrugations, thereby *decreasing* the threshold field from its value when the surfaces are flat. Recently Mirantsev showed theoretically [32,33] that a corrugation of the surface with a period of 1 μm and an amplitude of order 30 nm causes the surface-induced smectic layers to deform. This in turn leads to the suppression of the surface-induced smectic-A order parameter. Therefore, we would expect that a surface microrelief at one substrate would give rise to an effective thickness for the deformable region of a nematic cell that is greater than the effective nematic thickness when smectic order grows at both substrates.

Homeotropic cells were prepared by spin-coating a thick layer of the surfactant hexadecyltrimethylammonium bromide (HTAB) on a surface

layer of Nissan polyimide SE-1211, which itself was spin-coated on indium-tin-oxide (ITO) coated glass slides. (As an aside, we note that direct spin-coating of the HTAB/ethanol mixture onto the ITO resulted in randomly located pillars of surfactant (Fig. 10)—we refer to such a salt pillar as an **צידיח** ("ideet") [34]—which tended to break the stylus of the atomic force microscope (AFM) during the scribing process. To circumvent this problem the intermediate polyimide layer was added, which prevented formation of ideets). One surface was rubbed by the stylus of an atomic force microscope, creating grooves about 23 nm deep and having a period of 250 nm. The opposite side was not scratched. A cell of thickness (3.4 ± 0.1) μm was created and filled with the liquid crystal SCE12R (Merck), which has a negative dielectric anisotropy. Polarized light from a He-Ne laser passed through the cell, and was used to create an enlarged real image of the cell. Two spots in the cell were examined by passing the light from optical fibers into a pair of photodiode detectors. One fiber sampled the scratched region and the other fiber sampled the region just outside the scratch. As the a.c. electric field was ramped up slowly, the intensities at the two spots were recorded. We observed that the scratched region underwent a Fréedericksz transition at a lower threshold field than the outer region, which had two flat surfaces. Details of the experiment are

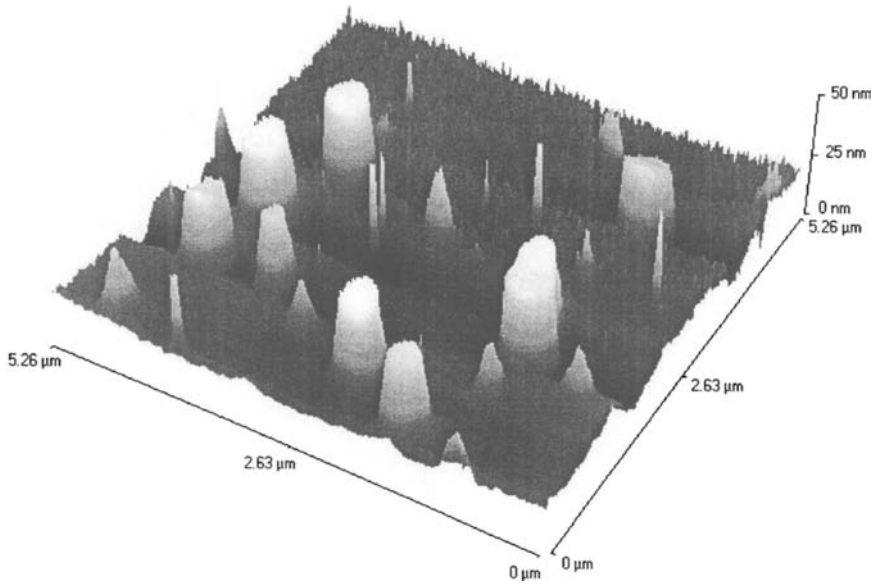

FIGURE 10 AFM micrograph showing pillars of HTAB surfactant, referred to as "ideets."

presented in Ref. [23]. Figure 11 shows the fractional decrease Φ in the threshold field as a function of temperature on approaching the nematic-smectic A phase transition from above. As expected, the *magnitude* of Φ increases toward T_{NA} due to the diverging smectic correlation length.

A detailed analysis of the data was performed according to the theory of Mirantsev; see Refs. [32] and [33] for details. In brief, the molecules and therefore the surface-induced smectic layers are forced to follow the surface corrugations. This requires the molecules to undergo a tilt with respect to the local layer normal, resulting in an energy cost. To reduce this energy cost, the smectic order is suppressed. In consequence, surface-induced smectic order grows into the bulk from the single flat substrate only, leaving a thicker elastically-deformable nematic region compared to the case of two flat substrates. Thus, the Fréedericksz threshold field is reduced. The dashed line in Figure 11 represents the theoretical fit. Based upon the fit, we were able to extract several material parameters. In particular, the tilt elastic constant D and the induced smectic order parameter was found to be considerably larger for SCE12R than for previous measurements with octylcyano biphenyl [31]. It is interesting to note that smaller surface corrugations would only partially reduce the degree of smectic order.

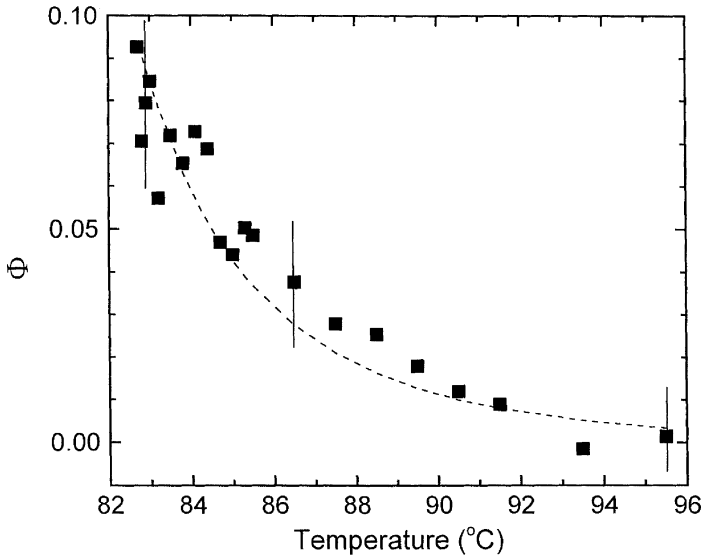

FIGURE 11 Dimensionless quantity Φ *vs.* temperature, showing the fractional decrease in Fréedericksz threshold field when only one surface (as opposed to both surfaces) are flat.

As a final example of a scientific application of nanolithography, we examine the controlled depression of the nematic – isotropic transition temperature due to elasticity and anchoring effects. In 1991 Barbero and Durand showed theoretically [35] that if the liquid crystal director attempts to follow the topography of a rough surface, the curvature elastic energy cost would result in a decrease of the nematic order parameter at the surface, or even melting into the isotropic phase. Several qualitative and semi-quantitative results for rough surfaces subsequently have been reported [36–38]. In contrast to surface topography, one also may examine this melting effect by using patterned easy axes *via* nanolithography. This technique relies on the anchoring properties of a substrate that is patterned for planar alignment, and thus is far easier to control than surface roughness.

To quantify the effects on the nematic – isotropic transition temperature T_{NI} due to a nanoscopically-varying planar director profile, we prepared two substrates coated with a polyimide and buffed them with a cotton cloth. We then scribed a herringbone pattern into a $100 \times 100\,\mu m$ square, overwriting the cloth rubbing in this region of one substrate. Each period of 200 nm contains two very long pixels, approximately 100 nm wide and 100 μm long. The pixels were scribed so that the easy axes in adjacent pixels make an angle ψ with respect to each other. The depression of T_{NI} at the patterned surface relative to its value at a uniformly-oriented surface was investigated as a function of ψ.

The cell, filled with the liquid crystal octyloxycyanobiphenyl (8OCB), was viewed using a polarizing optical microscope in the isotropic phase while being slowly cooled at a rate of $-4\,mK\,min^{-1}$. Owing to a temperature gradient of several tens of millikelvins per millimeter in the plane of the cell, a nematic – isotropic phase front moved across the cell with decreasing temperature. Additionally, a small vertical temperature gradient also was present. Because the nematic (rather than the isotropic) phase preferentially wets the polyimide-coated substrate independent of rubbing conditions, the observed "head" of the front corresponds to a nematic layer extending forward along the surface, in contact with the isotropic phase in bulk. We estimate the angle of the nematic layer to be < 0.05 rad, based upon the optical interference patterns observed in the nematic layer. It is important to note that this region corresponds to a nucleated nematic phase, rather than paranematic order. As the head of the nematic layer reached an AFM-scribed square, it became pinned at the boundary between the uniformly cloth-rubbed, nematic-friendly surface region and the AFM-scribed, nematic-hostile region. [The term "nematic-hostile" is relative: The nematic phase wets the polyimide-coated substrate, whether uniformly rubbed or scribed with a herringbone patterns. The herringbone pattern is just more hostile to the nematic phase than the uniformly rubbed

region]. We define temperature T_1 as the temperature at which the nematic layer just reached the square. With decreasing temeprature, the nematic layer continued to advance *outside* the square, but inside the region beneath the square the liquid crystal remained in the isotropic phase. Then at a temperature T_2 the nematic layer began to move into the square. We define $\Delta T \equiv T_1 - T_2$ as the difference in transition temperatures between the uniformly rubbed region and the herringbone region. It is important to note that we measured the temperature *difference*, not the absolute nucleation temperature. ΔT was determined to within 0.5 to 1 mK. Figure 12 shows the experimental results for three different thickness cells.

To understand the results, we note that the period of the herringbone is smaller than the extrapolation length K/W, where K is an appropriate elastic constant. Thus, the director is unable to closely follow the local easy axis, giving rise to both elastic and anchoring energy costs that penetrate into the nematic layer a distance of order the herringbone period. (In fact, calculations reveal that the penetration is an order of magnitude smaller than the period [39]). Calculating the elastic and anchoring energy and using the Kelvin equation [40], we find that the nematic layer at the front has a thickness of a few nematic correlation lengths. Moreover, we find that the anchoring energy plays the dominant role in the depression of T_{NI},

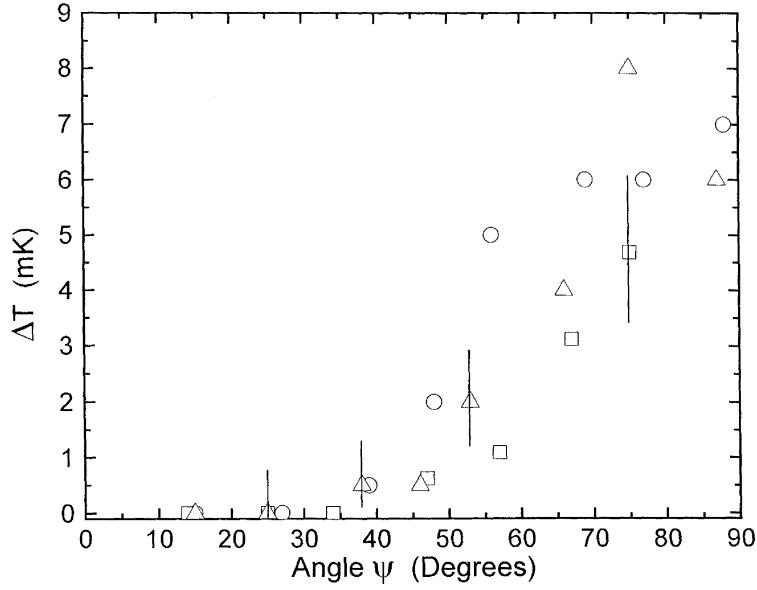

FIGURE 12 ΔT *vs.* ψ for three different thickness cells.

unlike the result in Ref. [35]. Details of the experiment and analysis will be published elsewhere [39].

Nanoscopic control of the surface will play an increasingly important role in both liquid crystal science and technology. I have outlined only a few of the topics that are possible using these techniques, although potential areas of study are limited only by the imagination.

REFERENCES

[1] Sarid, D. (1994). *Scanning force microscopy*, Oxford University Press: Oxford.
[2] Lewis, A., Isaacson, M., Muray, A., & Harootunian A, A. (1983). *Biophys. J.*, *41*, A405.
[3] Seo, D. S., Ohide, T., & Kobayashi, S. (1992). *Mol. Cryst. Liq. Cryst.*, *214*, 19.
[4] Seo, D. S., Ohide, T., & Kobayashi, S. (1992). *Mol. Cryst. Liq. Cryst.*, *214*, 97.
[5] Zhu, Y. M., Wang, L., Lu, Z. H., Wei, Y., Chen, X. X., & Tang, J. H. (1994). *Appl. Phys. Lett.*, *65*, 49.
[6] Skaife, J. J. & Abbott, N. L. (1999). *Chem. Mater.*, *11*, 612.
[7] Berreman, D. W. (1972). *Phys. Rev. Lett.*, *28*, 1683.
[8] Geary, J. M., Goodby, J. W., Kmetz, A., & Patel, J. S. (1987). *J. Appl. Phys.*, *62*, 4100.
[9] Mahajan, M. P. & Rosenblatt, C. (1998). *J. Appl. Phys.*, *83*, 7649.
[10] Mahajan, M. P. & Rosenblatt, C. (1999). *Appl. Phys. Lett.*, *75*, 3623.
[11] Kikuchi, H., Logan, J. A., & Yoon, D. Y. (1996). *J. Appl. Phys.*, *79*, 6811.
[12] Gu, D. F., Rosenblatt, C., & Li, Z., (1995). *Liq. Cryst.*, *19*, 489.
[13] Fang, J. Y., Lu, Z. H., Ming, G. W., & Wei, Y. (1993). *Liq. Cryst.*, *14*, 1621.
[14] Smith, D. P. E., Horber, H., Gerber, C., & Binnig, G. (1989). *Science*, *245*, 43.
[15] Hara, M., Iwakabe, Y., Tochigi, K., Sasabe, H., Garito, A. F., & Yamada, A. (1990). *Nature*, *344*, 228.
[16] Lee, B. W., Link, D. R., & Clark, N. A. (2000). *Liq. Cryst.*, *27*, 501.
[17] Rüetschi, M., Grütter, P., Fünfschilling, J., & Güntherodt, H.-J. (1994). *Science*, *265*, 512.
[18] Pidduck, A. J., Haslam, S. D., Bryan-Brown, G. P., Bannister, R., & Kietly, I. D. (1997). *Appl. Phys. Lett.*, *71*, 2907.
[19] Kim, J.-H., Yoneya, M., Yamamoto, J., & Yokoyama, H. (2001). *Appl. Phys. Lett.*, *78*, 3055.
[20] Bing Wen & Rosenblatt, C. (to be published).
[21] Bing Wen, Mahajan, M. P., & Rosenblatt, C. (2000). *Appl. Phys. Lett.*, *76*, 1240.
[22] Bing Wen & Rosenblatt, C. (2001). *J. Appl. Phys.*, *89*, 4747.
[23] Sinha, G. P., Rosenblatt, C., & Mirantsev, L. V. (2002). *Phys. Rev. E* , *65*, 041718–1.
[24] Bing Wen, Petschek, R. G., & Rosenblatt, C. (2002). *Appl. Optics OT*, *41*, 1246.
[25] Clark, N. (1985). *Phys. Rev. Lett.*, *55*, 292.
[26] Ouchi, Y., Feller, M. B., Moses, T., & Shen, Y. R. (1992). *Phys. Rev. Lett.*, *68*, 3040.
[27] Yamagachi, R. & Sato, S. (2000). *Jpn. J. Appl. Phys.*, *39*, L-681.
[28] Vetter, P., Ohmura, Y., & Uchida, T. (1993). *Jpn. J. Appl. Phys.*, *32*, L-1241.
[29] Feller, M. B., Chen, W., & Shen, Y. R. (199). *Phys. Rev. A*, *43*, 6778.
[30] Oh-Ide, T., Kuniyasu, S., & Kobayashi, S. (1988). *Mol. Cryst. Liq. Cryst.*, *164*, 91.
[31] Rosenblatt, C. (1984). *Phys. Rev. Lett.*, *53*, 791.
[32] Mirantsev, L. V. (1999). *Phys. Rev. E*, *59*, 5549.
[33] Mirantsev, L. V. (1997). *Mol. Cryst. Liq. Cryst. Sci. Technol., Sect. A*, *301*, 137.
[34] According to Midrashic tradition (*Midrash Tanchuma* in *Genesis*, *Veyeira Siman* 8), "Ideet" was the name of Lot's wife, the Biblical character who transformed into a pillar of salt when she looked back at the city of Sodom (*Genesis* 19:26).
[35] Barbero, G. & Durand, G. (1991). *J. Phys. II (France)*, *1*, 651.

[36] Barberi, R. & Durand, G. (1990). *Phys. Rev. A*, *41*, 2207.
[37] Papnek, J. & Martino-Lagarde, Ph. (1996). *J. Phys. II (France)*, *6*, 205.
[38] Monkade, M., Martino-Lagarde, Ph., Durand, G., & Grandjean, C. (1997). *J. Phys. II (France)*, *7*, 1577.
[39] Bing Wen, Kim, J.-H., Yokoyama, H., & Rosenblatt, C. (2002). *Phys. Rev. E*, *66*, no. 041502.
[40] Sluckin, T. J. & Poniewierski, A. (1990). *Mol. Cryst. Liq. Cryst.*, *179*, 349.